fibers

MDPI

Article

Multi-Scale Toughening of UHPC: Synergistic Effects of Carbon Microfibers and Nanotubes

J. D. Ruiz Martínez [1], J. D. Ríos [2], H. Cifuentes [2,*] and C. Leiva [1]

[1] Department of Chemical and Environmental Engineering, Escuela Técnica Superior de Ingeniería, Universidad de Sevilla, 41092 Seville, Spain; jruiz3@us.es (J.D.R.M.); cleiva@us.es (C.L.)
[2] Department of Continuum Mechanics and Structural Analysis, Escuela Técnica Superior de Ingeniería, Universidad de Sevilla, 41092 Seville, Spain; jdrios@us.es
* Correspondence: bulte@us.es

Highlights

What are the main findings?

- Ultra-High Performance Concrete (UHPC) was reinforced at multiple scales using carbon microfibers and carbon nanotubes without compromising workability.
- This hybrid reinforcement increased compressive strength by 39%, tensile strength by 313%, and reduced macroporosity by 42%.

What is the implication of the main finding?

- The multi-scale reinforcement improves UHPC durability and fracture resistance.
- The carbon-based reinforcement offers a corrosion-free alternative for offshore and marine structures.

Abstract: This study investigates multi-scale reinforcement of Ultra-High-Performance Concrete through targeted modifications of its mechanical and fracture-resistant properties via carbon microfibers and carbon nanotubes. The research employed comprehensive characterization techniques including workability tests, mercury porosimetry for microscale porosity analysis, and X-ray tomography for macro-scale pore evaluation. Mechanical performance was assessed through compression strength, tensile strength, and fracture energy measurements. Results demonstrated significant performance enhancements testing UHPC samples with 6 mm carbon microfibers (9 kg/m^3) and varying carbon nanotubes dosages (0.11–0.54 wt%). The addition of carbon microfibres improved compressive strength by 12%, while incorporating 0.54 wt% carbon nanotubes further increased strength by 24%. Remarkably, the combined reinforcement strategy yielded a 313% increase in tensile strength compared to the reference mixture. The synergistic effect of carbon fibers and carbon nanotubes proved particularly effective in enhancing concrete performance. This multi-scale reinforcement approach presents a promising alternative to traditional steel fiber reinforcement, offering superior mechanical properties and potential advantages in corrosive environments.

Keywords: ultra-high-performance fiber-reinforced concrete; thermogravimetric analysis; carbon microfiber; carbon nanotubes; fiber–matrix interaction

check for updates

Academic Editor: Ramiro Rafael Ruiz Rosas

Received: 13 February 2025
Revised: 11 March 2025
Accepted: 15 April 2025
Published: 21 April 2025

Citation: Martínez, J.D.R.; Ríos, J.D.; Cifuentes, H.; Leiva, C. Multi-Scale Toughening of UHPC: Synergistic Effects of Carbon Microfibers and Nanotubes. *Fibers* **2025**, *13*, 49. https://doi.org/10.3390/fib13040049

Copyright: © 2025 by the authors. Licensee MDPI, Basel, Switzerland. This article is an open access article distributed under the terms and conditions of the Creative Commons Attribution (CC BY) license (https://creativecommons.org/licenses/by/4.0/).

1. Introduction

Ultra-High-Performance Concrete (UHPC) is one of the most representative cement-based composite materials, characterized by its high compressive strength, remarkable

tensile strength, and excellent durability. UHPC is distinguished by a water/cement ratio often below 0.2 and the integration of very fine cementitious materials and supplementary aggregates to promote the hydration process and form a low porosity structure [1–7]. This meticulous composition results in a denser matrix that minimizes potential failure points over the life of the material [6–8]. The incorporation of short fibers such as steel, carbon, glass, PVA, and polypropylene fibers among the most used is a strategic response to improve ductility, energy absorption, and tensile strength [9–13]. These fibers are essential for crack resistance, as they act as a unifying force across cracks [13–16].

Carbon fiber (CF)-reinforced UHPC has emerged as a promising material for advanced structural applications, especially in marine environments. Similarly to other fibers, the inclusion of CF can bridge micro-cracks in UHPC, allowing the material to continue to support the load after cracking due to the high strength of the bond between the carbon fiber and the cement-based material [17,18]. The optimal length of CFs in UHPC typically ranges from 3 to 6 mm, which allows for improved dispersion [17,19]. CF reinforcement of UHPC offers several advantages over traditional steel fibers, such as higher tensile strength, corrosion resistance, lower diameter, and lower weight [17,20,21]. This makes it particularly suitable for offshore wind turbine foundations, where resistance to harsh marine conditions is crucial [19,21]. The non-corrosive nature of CFs eliminates the risk of reinforcement degradation in saltwater environments, which can extend the life of offshore structures [19,21]. In addition, the use of recycled CFs in UHPC has shown promise for cost reduction and improved sustainability, while maintaining attractive mechanical properties [17].

Nanotechnology has revolutionized the development of UHPC, emerging as promising reinforcement material [22–24]. Nanomaterials significantly influence UHPC's microstructural development and performance characteristics. Their effectiveness as reinforcement depends on multiple factors including morphology, dimensions, surface characteristics, bond strength with the matrix, and capacity for crack control and energy absorption [24]. The deterioration process in cementitious materials typically begins with nanocracks, which progressively develop into micro- and macroscale defects, compromising both mechanical properties and durability [24,25]. Recent advances in concrete technology have explored various nanomaterials including carbon nanotubes (CNT), graphite nanoplatelets (GNP), nano silica (NS), Al_2O_3 nanofiber (ANF), and graphene oxide (GO), among others. These materials, when optimally incorporated, enhance both mechanical properties and matrix density through distinct mechanisms. Inert nano additives function via nucleation, filling, and bridging effects, while active nanomaterials provide these benefits while also accelerating hydration kinetics. However, careful dosage control is crucial, as excessive quantities can lead to agglomeration and reduced workability, ultimately increasing porosity [23,26,27].

Regarding CNTs, Jung et al. [28] evaluated the impact of dispersed multi-wall CNTs on the compressive strength and elastic modulus of UHPCS, finding both approaches effective. Electrically cured UHPC with 1.2 wt% CNTs achieved the highest compressive strength and elastic modulus, 8.6% and 17.1% higher, respectively, compared to steam-cured UHPC without CNTs. It was also found that the incorporation of CNTs enhanced the strength of concrete by creating bridges between hydration products and forming cross-linked networks within the C–S–H silicate chains, thus limiting microcrack development [29]. This improvement is attributed to CNTs strengthening hydration products and forming denser C–S–H agglomerates with higher stiffness and filling macro and micro-pores [26,30,31]. Viana et al. [32] observed strength increases at CNT dosages of 0.05–0.1% by weight of cement, while Zhang et al. [33] reported similar trends for dosages up to 0.05%. CNTs also enhance residual strength and reduce spalling at high temperatures (up to 300 °C)

by creating pore structures that allow vapor escape and by reinforcing the matrix. Ozone-treated CNTs improved UHPC compressive strength by 30.6% and 9.8% at 1 and 28 days, respectively, at a dosage of 0.1 wt% [34]. Ruan et al. [35] reported increased strength and toughness with CNT dosages up to 0.5%, regardless of length variations. Regarding the importance of CNT dispersion, Chen et al. [30] state that poor dispersion causes defects and increases porosity and propose ultra-sonic dispersion as a solution. Ultrasonic Dispersed CNTs (0.25–0.5%) enhanced dynamic compressive strength, impact toughness, and energy dissipation under high strain rates (200–800/s), with improvements of 68.9–71.0% at 0.5% dosage [36].

The UHPC developed in this study has significant potential for a wide range of structural applications, particularly those requiring high strength, durability, and resistance to harsh environments. Key applications include offshore and marine structures (e.g., wind turbine foundations and coastal bridges), blast- and impact-resistant buildings, long-span bridges, high-rise buildings, precast concrete elements, and seismic-resistant structures. The non-corrosive nature and lightweight properties of CFs and CNTs make this material particularly suitable for sustainable infrastructure projects, where durability and reduced maintenance are critical [21].

This study investigates the multiscale interaction between CNTs and carbon microfibers in enhancing UHPC. By testing UHPC samples with 6 mm CFs and varying CNT dosages, we evaluated mechanical properties and fracture behavior, linking fiber and nanoparticle effects to matrix pore structure and overall performance. Advanced X-ray computed tomography and mercury intrusion porosimetry provided data of the internal pore network, while scanning electron microscopy (SEM) revealed detailed insights into the fiber–concrete interface and failure mechanisms. Combining these analyses with mechanical testing, it was possible to identify how microstructural changes driven by fiber reinforcement improve the strength and durability of UHPC.

2. Materials and Methods

2.1. Materials

Figure 1 illustrates the materials used in this study, including cement, silica fume, aggregates, carbon fibers (CF), and carbon nanotubes (CNTs). Three components have been used as binder materials in this study: Type I cement 52.5 R/SR, manufactured by Portland Valderribas; silica fume (SF) S-92-D provided by SIKA; as well Arcelor-Mittal's ground granulated slag (GGS). Regarding aggregates, two types of quartz sand with different grain sizes have been used. Fine sand (FS) has a maximum grain size of 0.315 mm, while coarse sand (CS) is less than 0.800 mm.

To analyze the chemical composition of the cement materials, an X-ray fluorescence spectrometer was used. The results showed that the most abundant compounds were calcium oxide (CaO) and silicium dioxide (SiO_2); the remaining compounds and their proportions are detailed in Table 1. A superplastic (20HE) from Sika has also been incorporated. Carbon microfibers of the type TenaxTM HTC124, provided by Teijin CF, were used with the following characteristics: a diameter of 7 μm, a length of 6 mm, a tensile strength (f_t) of 4200 MPa, and a Young's modulus (E) of 230 GPa. Carbon nanofibers (CNTs) from Sigma-Aldrich were used, with the following characteristics: a diameter of 100 μm and a length mostly within the range of 20 to 80 μm.

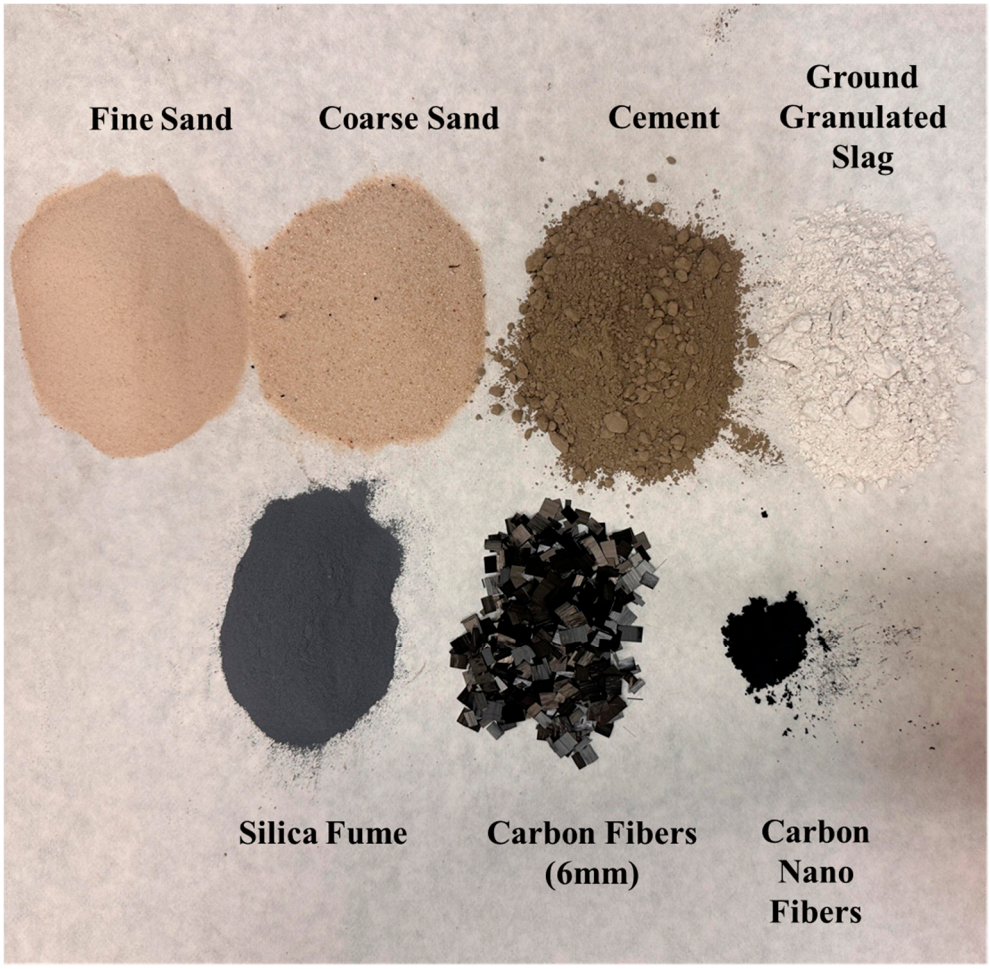


Figure 1. Materials used in the UHPC formulations.

Table 1. Chemical composition by FRX of the bonding materials.

	Portland Cement	GGBS	SF
Al_2O_3	6.59	9.83	0.20
BaO	0.06	-	-
CaO	45.61	35.12	0.30
Cl_2O_3	0.07	-	-
CuO	0.04	-	-
Fe_2O_3	2.85	0.31	0.06
K_2O_2	1.09	2.01	0.42
MgO	1.00	6.63	0.35
MnO_2	0.05	0.11	-
NaO_2	0.29	0.21	0.12
P_2O_5	0.13	-	-
SiO_2	18.29	27.81	79.58
SO_3	4.02	-	-
SrO	0.05	0.08	-
TiO_2	0.41	0.48	-
ZnO	0.02	-	-

2.2. Mix Proportions and Specimen Preparation

Five distinct mixtures of UHPC were developed, as shown in Table 2. The CF dosage was chosen based on prior studies [37], as it provides an optimal balance between workability, porosity, and mechanical performance. Higher CF contents tend to reduce workability,

while lower dosages offer limited mechanical benefits. In contrast, the CNT dosage was varied to assess its effect on microstructural refinement and mechanical properties, ensuring proper dispersion through preliminary trials The effect of both microfibers and CNTs was analyzed across the different formulations. The total solid content in the matrix was the same for all mixtures. The amount of CF (9 kg/m^3) remained the same in four out of the five mixes, but different concentrations of CNT were used (0, 0.11, 0.32 and 0.54 kg/m^3). The mixtures were named D*n-m*, where *n* is the dosage of microfiber (kg/m^3), and *m* is the dosage of nanotubes (kg/m^3), resulting in the following formulations: D0-0, D9-0, D9-0.11, D9-0.32, D9-0.54.

Table 2. Components and compositions of all mixtures (kg/m^3).

Component (kg/m^3)/Mixture	D0-0	D9-0	D9-0.11	D9-0.32	D9-0.54
Cement	540.07	540.07	540.07	540.07	540.07
Silica Fume	210.09	210.09	210.09	210.09	210.09
GGS	310.02	310.02	310.02	310.02	310.02
FS	470	470	470	470	470
CS	470	470	470	470	470
Water	199.33	199.33	199.33	199.33	199.33
Superplasticizer	44.4	44.4	44.4	44.4	44.4
CF	-	9	9	9	9
CNT	-	-	0.11	0.32	0.54

In the first stage, the solid components (cement, SF, GGBS, FS, and CS) were placed into a vertical mixer and mixed for 5 min. In a parallel way, the water, superplasticizer, and carbon nanofibers were sonicated using an UltraSons 300515 ultrasound device for 15 min to obtain a homogeneous liquid mixture; this time was determined to be optimal in terms of dispersion in previous studies [38]. Subsequently, the solid and liquid components were combined and mixed for 20 min. Finally, the CFs were added and mixed for 5 min to achieve the appropriate consistency. Three prisms (40 × 40 × 160 mm^3) were manufactured from each mixture (Figure 2). For each mix, six specimens were tested, prepared in two separate batches to verify reproducibility and ensure consistent results. After 24 h, the samples were removed from the molds and subjected to a water curing process at room temperature for 28 days. Then, the samples were left to dry for 24 h before being tested.

2.3. Experimental Program

2.3.1. Workability

To evaluate the workability of fresh concrete, a miniaturized slump test was conducted following the procedures outlined in the EN 12350-2:2020 standard [39]. The test setup utilized a modified Abrams cone with dimensions of 50 mm at the top, 100 mm at the bottom, and 150 mm in height, aligning with the methodology described by Nguyen et al. [40].

2.3.2. Pore Size Distribution Through X-Ray Computed Scan and Mercury Porosimetry

X-ray computed tomography was employed to evaluate macrostructural modifications induced by the incorporation of CFs and CNTs. The investigation utilized a YXLON Y. Cougar SMT X-ray system, located at the University of Seville's X-ray Characterization Service. The experimental protocol involved scanning three representative samples for each concrete mixture, generating a total of 12 CT scans. Statistical analysis captured the mean values and microstructural deviation. Sample dimensions were standardized at 8 × 8 × 4 mm^3. Pore characterization was conducted using Dragonfly software (version 2022.2), which differentiates concrete matrix constituents based on their inherent

density variations. A comprehensive methodology for porosity analysis via X-ray CT has been previously documented by Ríos et al. [8,41]. Given the specific experimental conditions—equipment specifications, concrete typology, and sample geometry—the X-ray measurement precision was estimated at approximately 40 µm.



Figure 2. Manufactured specimens before being tested.

For smaller porosity measurements, porosimetry was conducted using a Micromeritics Autopore IV 9500 mercury intrusion porosimeter (Norcross, GA, USA). The analysis encompassed a comprehensive pore size range from 0.007 µm to 150 µm, enabling detailed characterization of the material's microstructural properties. Sample preparation involved obtaining 5 mm diameter cylindrical pellets, which were subsequently subjected to controlled thermal drying in a laboratory oven. Specimens were maintained at a constant temperature of 105 °C until achieving a stable mass, ensuring consistent and reproducible analytical conditions.

2.3.3. Thermogravimetric Analysis (TGA)

Thermogravimetric characterization was performed utilizing a Mettler-Toledo TG-SDTA 851 thermogravimetric analyzer (Columbus, OH, USA), examining material transformations across a temperature spectrum ranging from ambient conditions to 1000 °C. Surface-extracted specimens, carefully selected with masses between 100 and 150 mg, underwent comprehensive thermal analysis. The experimental protocol employed atmospheric air as purge gas, maintaining a consistent heating progression of 10 °C per minute to ensure systematic and controlled thermal evaluation.

2.3.4. Scanning Electron Microscopy (SEM)

In order to better understand the role of defects, particularly those that may be pre-sent at the fiber/matrix interface and the influence of the CF, a sample was analyzed with a Hitachi S5200 scanning electron microscope (SEM, Tokyo, Japan).

2.3.5. Mechanical Properties

Compressive Strength

Compressive strength evaluation was conducted on six specimens for each mixture configuration, with standardized dimensions of 80 × 40 × 40 mm^3. Testing procedures strictly adhered to the EN 12390-3 standard [42]. A servo-hydraulic testing apparatus with a 3000 kN load capacity was employed to execute the comprehensive mechanical characterization.

Tensile Strength

A three-point bending test was conducted on prismatic specimens measuring 40 × 40 × 160 mm^3, following the RILEM TCM-85 [43] protocol, to determine fracture work and fracture energy. Mechanical testing was performed utilizing a servo-hydraulic testing system configured with a maximum load capacity of 200 kN, employing Crack Mouth Opening Displacement (CMOD) as the primary displacement control mechanism. To mitigate potential torsional deformation and ensure experimental precision, anti-torsion stabilization devices were strategically implemIented on both the loading and support rollers. The notch geometry was standardized with a length-to-depth ratio of one-sixth for all test specimens (Figure 3). Note that the bilinear approximation of the tension-softening diagram (Figure 4) yields a value for the concrete's direct tensile strength (f_t).

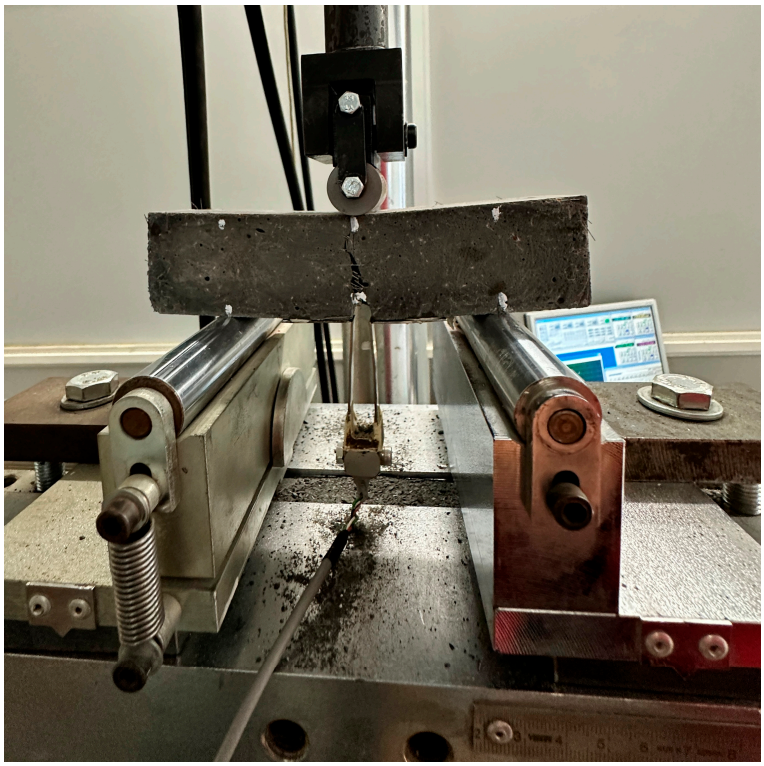


Figure 3. Three-point bending test.

Fracture Behavior

Fracture energy and cohesive law parameters were obtained through inverse analysis. The inverse analytical methodology involved iteratively calibrating cohesive law parameters to optimize the correspondence between experimentally derived load–CMOD curves and the theoretical cohesive model's load–CMOD representation (Figure 4). Based on the non-linear hinge model [44,45], the cohesive law was conceptualized as a bi-linear framework, strategically segmented into two distinct branches: the first branch characterized

by fracture energy—yellow color—(G_f), and the second branch defined by the residual fracture energy—blue color—($G_F - G_f$).

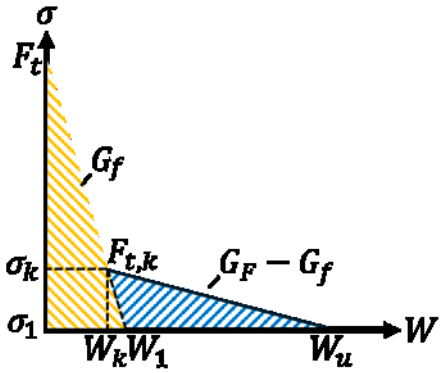


Figure 4. Bilinear cohesive law of fracture process.

3. Results and Discussion

3.1. Thermogravimetric Analysis

Thermogravimetric analysis (TGA) was performed on D9-0 and D9-0.32 samples to examine material transformations with and without nanofiber addition. Figure 5 illustrates the thermogravimetric and differential thermogravimetric curves from ambient temperature to 1000 °C. Three distinct thermal decomposition peaks were identified within the temperature ranges of 100–200 °C, 400–500 °C, and 500–600 °C, revealing the characteristic material response to progressive thermal loading.

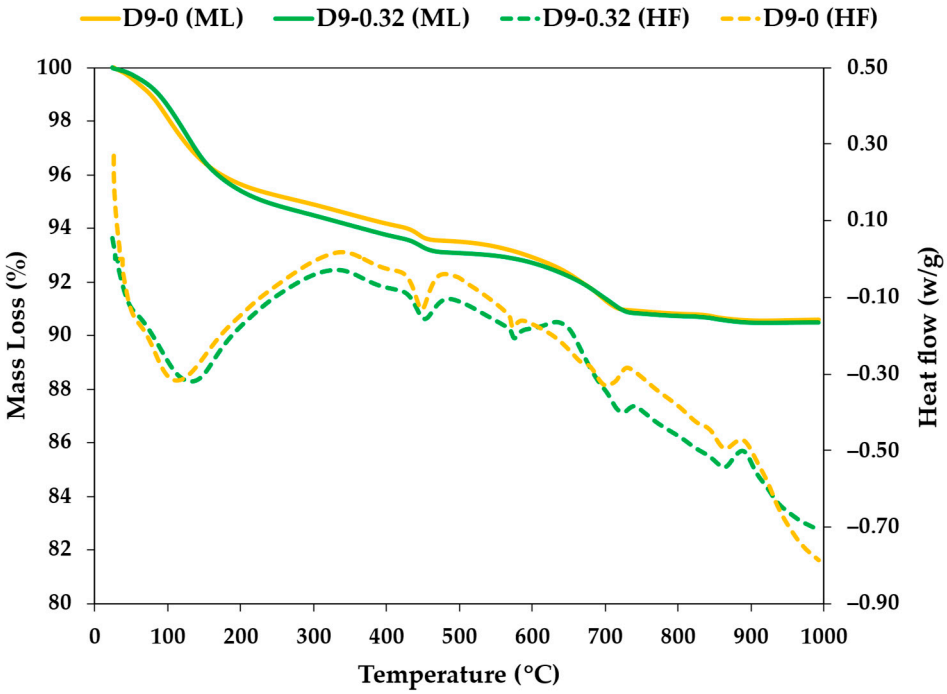


Figure 5. TGA comparison of UHPC reinforced with CFs and CNTs.

The initial thermal peak (100–200 °C) represents moisture and capillary water evaporation, alongside C–S–H gel dehydration. CNTs are chemically inactive and do not participate in hydration reactions, but their incorporation serves as nucleation sites for the formation of denser C–S–H structures while simultaneously filling pores at multiple scales [26,46], thereby accelerating the development of hydration products, including C–S–H and calcium hydroxide.

The second mass loss reaction occurs between 500 °C and 600 °C, corresponding to the dihydroxylation of calcium hydroxide ($Ca(OH)_2$). This stage exhibits a 0.53% mass loss variation, showing that CNT addition slightly increases mass loss due to a higher concentration of $Ca(OH)_2$, the main pozzolanic reactant (with fly ash, SF, or GGBS) in the formation of additional C–S–H gel [47]. These outcomes are in line with Fu et al. [48], who reported that the proportions of gel pores and innocuous capillaries, as well as the amount of hexagonal prismatic $Ca(OH)_2$, rose with the addition of CNTs.

In the third stage, referring to calcium carbonate ($CaCO_3$) decomposition, the same trend is observed but with a less significant 0.3% mass loss variation. Again, the D9-0.54 mix shows a more pronounced peak due to its higher $CaCO_3$ concentration, which helps densify the concrete [49]. Reactions after 700 °C relate to the loss of residual hydroxides, and there is no significant difference between the mixes reaching the same mass loss towards the end of the TGA [50].

3.2. Workability

The results assessing the workability of each mixture are shown in Figure 6. The results indicated a clear trend: the inclusion of CFs led to a reduction in slump diameter. Moreover, the results demonstrated that increasing the carbon nanotube dosage resulted in lower workability.

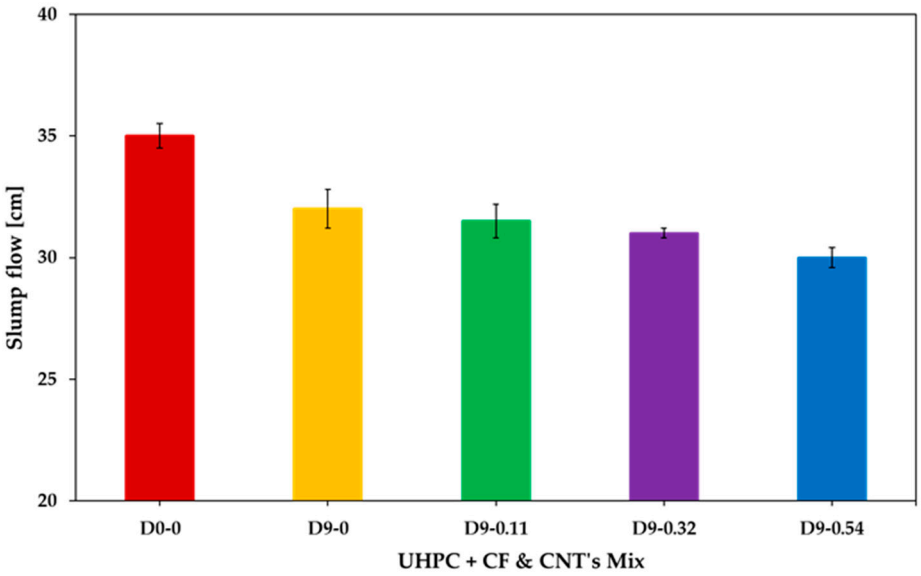


Figure 6. Workability slump test.

As depicted in Figure 4, the incorporation of CF leads to a 9% reduction in workability. This phenomenon can be attributed to the CF's ability to create a significantly denser matrix, which largely explains the more substantial workability reduction. The workability loss becomes less pronounced with CNT addition, ranging from 11% to 14% relative to the reference mixture (D0-0). The irregular morphology of carbon nanotubes contributes to enhanced inter-component cohesion within the mixture. Nevertheless, it is noteworthy that all investigated mix designs maintain self-compacting characteristics (>28 cm), demonstrating their inherent ability to fill molds through gravitational forces alone, without the need for external compaction.

3.3. Pore Size Distribution Through X-Ray Computed Scan and Mercury Intrusion Porosimetry (MIP)

X-ray tomography can size a range of macroporosity between 0.100 mm and 5 mm [41]. As shown in Figure 7, the concrete matrices exhibit macropore distributions ranging between 0.1 and 1.5 mm. The incorporation of CFs substantially reduced the quantity of macropores within the material matrix, while the addition of CNTs resulted in a residual decrease in total macroporosity.

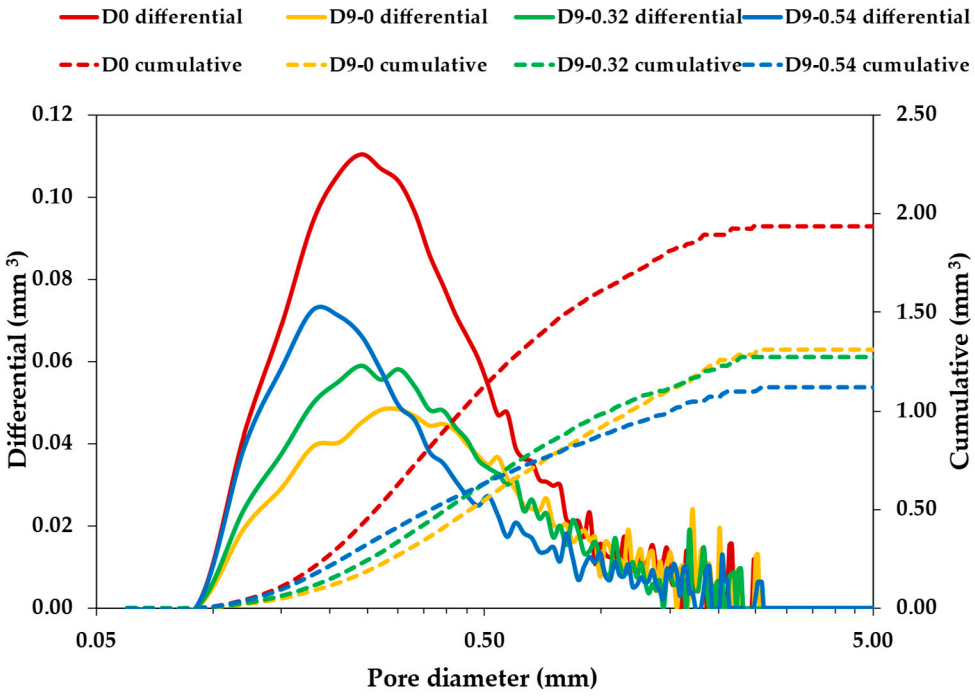


Figure 7. Macropore size distribution obtained by x-ray tomography.

Due to the reduced workability (Figure 6) induced by the CFs and CNTs, a slight increase in porosity between 0.1 and 0.3 mm was observed when CNTs were introduced (D9-0.54). Notably, in the larger pores (between 0.5 and 1.5), a significant decrease in the performance of the D9-0.54 mix was observed, while the reference samples D0-0 and D9-0 showed the highest amount of large pores, which demonstrates the effective role of CNTs in pore reduction and enhancing matrix densification. These results are in line with the outcomes described in the TGA (Figure 5).

Overall, the combined effect of the multi-scale reinforcement resulted in better performance in terms of total macroporosity. The addition of microfibers achieved a 32% reduction (D0 vs. D9-0), while the incorporation of CNTs at higher nanofiber concentrations (0.54 kg/m^3) further reduced the cumulative macroporosity by up to 42% (D9-0 vs. D9-0.54). These outcomes suggest the creation of a denser concrete matrix, which can potentially inhibit crack initiation during the fracture process.

Once the distribution of macroporosity has been established, MIP allows us to assess the distribution of smaller pores. The concrete's MIP results can be categorized into three distinct types: (a) nanopores with dimensions ranging from 0.005 to 0.01 μm; (b) micropores with mean radio from 0.01 to 10 μm, primarily representing the water-filled spaces between original cement grains; and (c) mesopores larger than 10 μm, predominantly formed by entrapped air [8].

The results depicted in Figure 8 indicate that plain concrete exhibits a high volume of micro- and mesopores, as corroborated by the larger pore sizes and greater cumulative macroporosity observed for the D0-0 mixture in x-ray tomography (Figure 7). When CFs

are incorporated, a reduction in the volume of mesopores is observed. This reduction is even more significant with the addition of CNTs, as demonstrated by a D9-0.54 mix, which shows the lowest mesopore content.

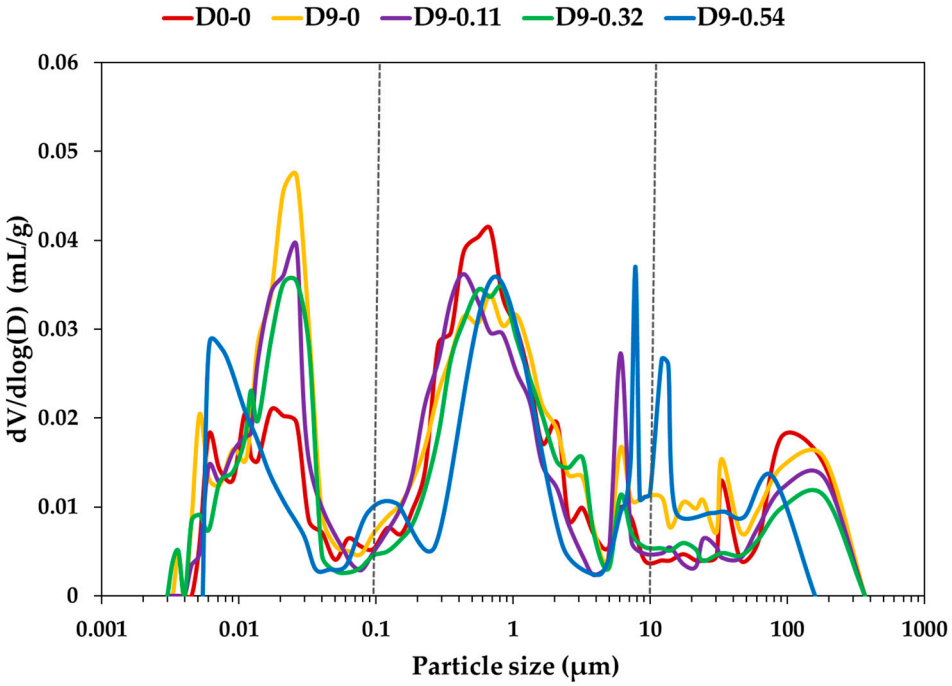


Figure 8. Mercury intrusion porosimetry results.

While the addition of CFs increases the volume of nanopores within the cementitious matrix, this increase is less pronounced when CNTs are also present. The CFs appear to act as tiny mixing aids, helping to reduce the larger pores in the concrete during the mixing process, as previously reported in other studies [8,51]. Overall, the multi-scale reinforcement strategy involving both CFs and CNTs effectively modifies the concrete's pore structure, leading to a more dense and less porous matrix, which can positively impact the material's strength and durability. This has the potential to reduce seawater penetration and improve the performance of UHPC in applications such as offshore turbines [52].

3.4. Mechanical Properties

3.4.1. Compressive Strength

Figure 9 illustrates the compressive strength progression of concrete specimens with varying CF and CNT concentrations. The initial sample (D0-0) demonstrated a baseline strength of 91 MPa, which increased to 102 MPa (12% improvement) upon CF addition. Subsequent CNT incorporation revealed a consistent strength enhancement pattern: the D9-0.11 sample reached 112 MPa (8% increase vs. D9-0); D9-0.32 achieved 120 MPa (17% increase vs. D9-0); and the highest concentration sample exhibited 127 MPa (24% increase compared with D9-0), a total increase of 39% compared with UHPC reference.

Regarding the strength enhancement mechanism, the improvements observed are attributed to the unique interactions of CF and CNTs within the concrete matrix. CFs create robust interfacial bonds, refine microstructural characteristics, and effectively bridge and deflect macrocracks, as illustrated in Figure 10 [48]. CNTs, on the other hand, promote uniform stress distribution, help eliminate entrapped air, and reduce internal microcracks (Figure 8). The progressive strength increase demonstrates the potential of both CFs and CNTs to significantly enhance concrete's mechanical performance.

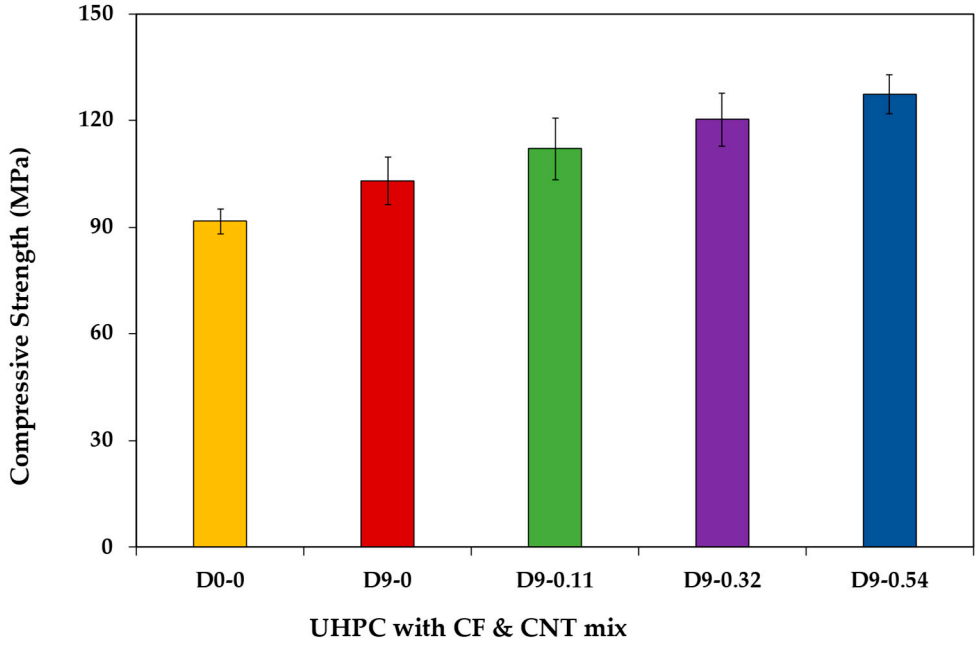


Figure 9. Compressive strength of each mix.

3.4.2. Fracture Behavior

When concrete fractures, a region called the Fracture Process Zone (FPZ) (Figure 10) forms, as described by Swartz [53]. This zone involves various processes, including the development of microcracks, their coalescence, fissure branching, and friction between fractured surfaces. These phenomena occur within the Interfacial Transition Zone (ITZ), a weak area located between sand grains and the cement paste [41]. Prior to crack formation, stresses build up in the FPZ, with a strength comparable to concrete's tensile resistance. These stresses gradually diminish to zero at the outer boundary of the FPZ, following Hilleborg's cracking model [54]. The fracturing mechanism in fiber-reinforced UHPC exhibits distinct characteristics compared to conventional concrete. One key factor is the significantly smaller aggregate size, approximately 100 times smaller than that in traditional concrete. This reduced size enhances material interaction, promotes a more uniform load distribution, and increases the concrete's deformation capacity prior to fracture.

Additionally, the inclusion of fibers in the matrix plays a critical role in crack initiation and propagation. As mentioned above, the fibers create a bridging effect, which modifies both the total porosity and the pore size distribution, especially macroporosity (as shown in Figure 7). This adjustment directly enhances the ability of fiber-reinforced concrete to absorb energy during the fracture process. In addition to strengthening the link between CFs and the cement matrix, CNTs on the cement matrix structure also strengthened the bond between the aggregate and the matrix. Therefore, adding CNTs and CFs to concrete greatly increases its resistance to fracture expansion, regardless of the strain rate. The crack expansion path became more curved, and crack penetration decreased significantly [48].

Figure 11 demonstrates the positive impact of CFs and the optimized combination of CFs and CNTs on the fracture energy performance of UHPC. The UHPC sample containing only CFs (D9-0) showed a significant increase in fracture energy, reaching a maximum of 260 N/m. This represents a 333% increase compared to the baseline D0-0 sample, which had an average of 78 N/m. When retaining the same microfiber content but incorporating different CNT portions, further improvements were observed. The D9-0.11 sample, with 0.11 kg/m^3 of CNTs, reached 288 N/m, an 11% increase over D9-0. The D9-0.32 sample exhibited the optimal fracture energy (291 N/m), a 12% improvement over D9-0. However, the high CNT content in the D9-0.54 sample led to a decrease in fracture energy to

232 N/m, an 11% reduction compared to D9-0. We could relate these results to the trend in macro-porosity (Figure 7), especially in pores between 0.1 and 0.3 mm. where the adverse trend shown in Figure 11—the higher amount of pores between these diameters—shows a worse performance in fracture energy. This was likely due to the adverse effects of excessive CNTs on workability that could have difficulted the fiber distribution, although their higher dosage achieves better mechanical performance, creating more resistance to crack propagation.

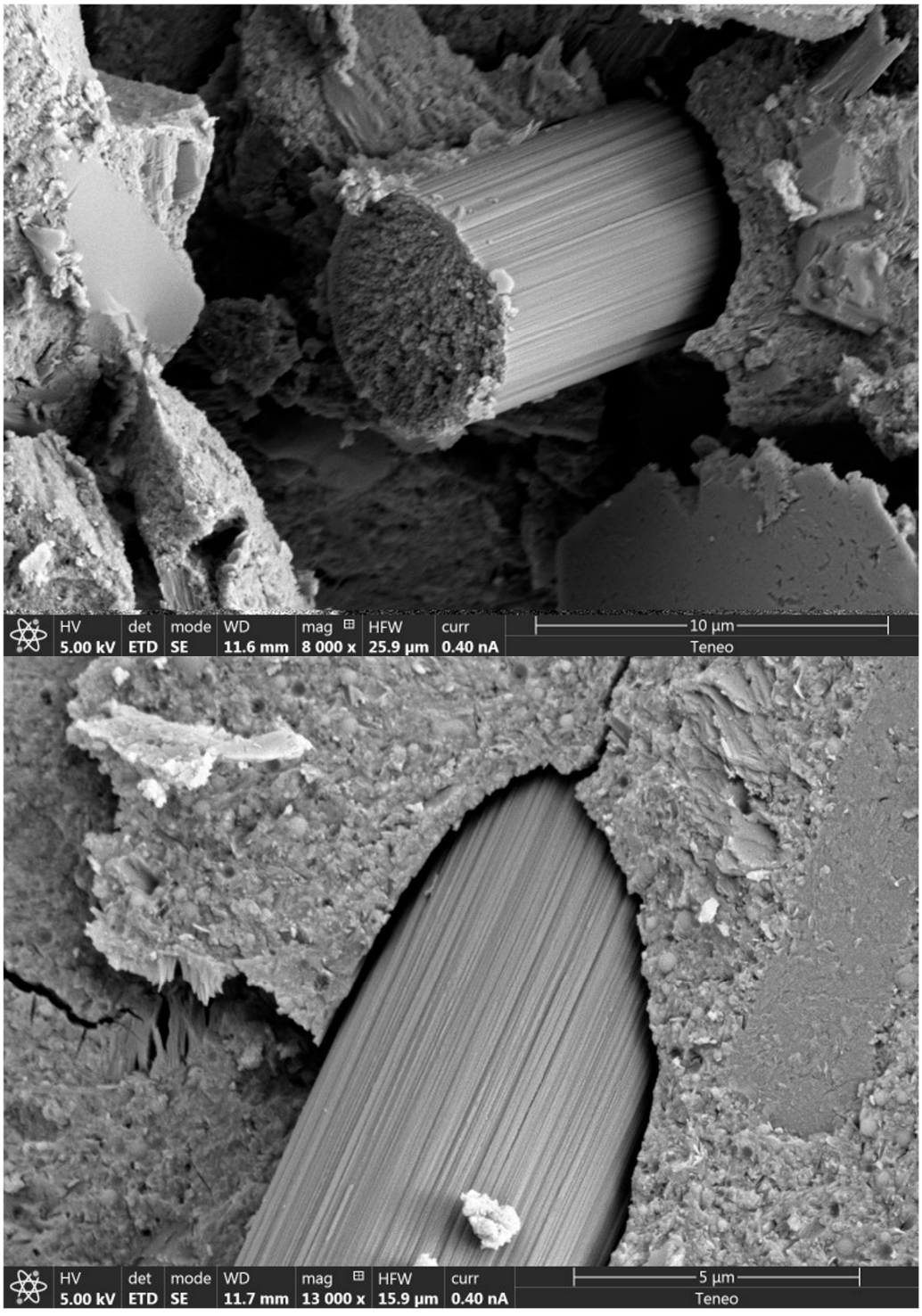


Figure 10. SEM images of the FPZ and ITZ of the D9-0 mixture.

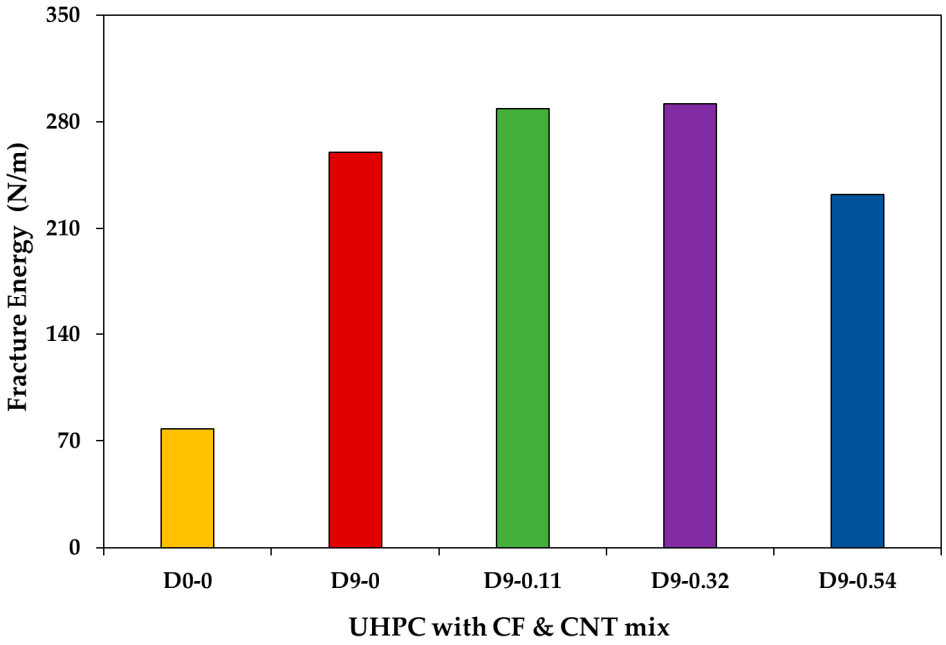


Figure 11. Fracture energy of each mix.

Figure 12 presents the failure modes of the tested specimens under compression. The image shows, from left to right, the mixes: D0-0, D9-0, D9-0.32, and D9-0.54. A clear trend can be observed: specimens exhibited an explosive failure under compression but with reduced damage due to the presence of CF. Furthermore, the densifying effect of the CF and CNT combination resulted in a more controlled fracture behavior, reinforcing the positive synergy between these materials.

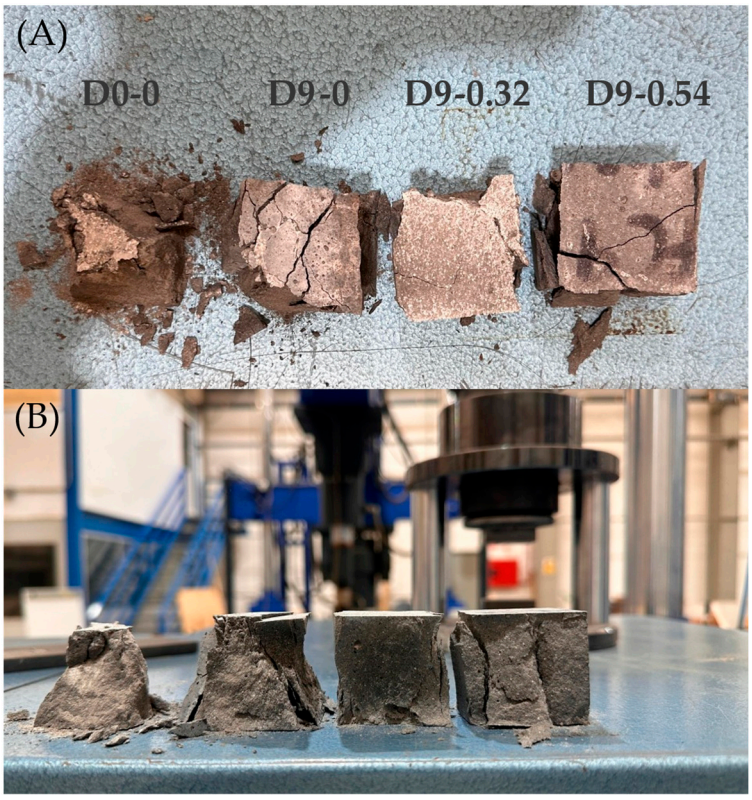


Figure 12. Test specimens tested for compressive strength (**A**) Top view (**B**) Side view.

3.4.3. Tensile Strength

The analysis of tensile behavior utilized bi-linear diagrams (Figure 2) derived from load–deflection curves using non-linear hinge modeling, with tensile resistance values obtained through cohesion law adjustments. The stress–displacement (σ–w) relationship exhibited two key phases: the initial linear segment (corresponding to tensile strength values shown in Figure 13) reflecting the combined effects of matrix microstructure and fiber bridging [55], followed by a second phase characterized by fiber pull-out behavior [56]. Standard deviation data are not available for these measurements.

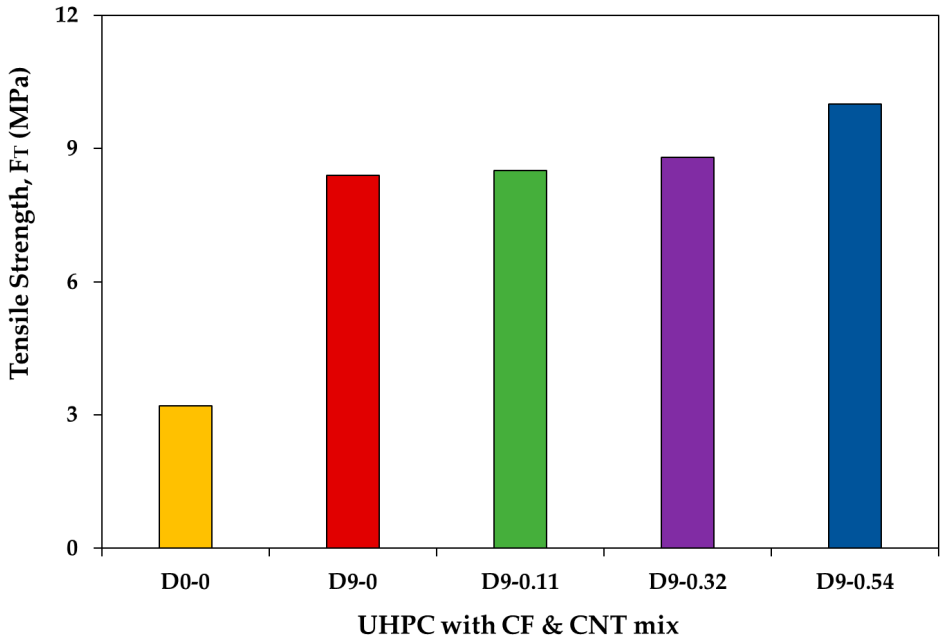


Figure 13. Tensile strength of each mix.

The results indicate that incorporating 9 kg/m^3 of fibers increased the tensile strength of the D9-0 mix (with 6 mm fibers) by 263% compared to the non-fiber concrete D0-0, which had a tensile strength of 3.2 MPa. This significant improvement is likely due to the high aspect ratio (length to thickness) of the CF, which increases the contact surface area between the fibers and surrounding cementitious matrix, enabling more effective crack bridging [29,48].

In contrast, mixes with both CFs and CNTs showed more modest improvements. D9-0.11 and D9-0.32 had only 1% and 5% increases in tensile strength over D9-0. However, D9-0.54 had notable 19% and 313% increases compared to D9-0 and D0-0, respectively. This aligns with the compressive strength linked to macro/micro porosity (Figures 7 and 8)—CF densifies the matrix, while CNTs reduce >0.1 mm pores (Figure 6), increasing fracture toughness.

4. Discussion

While previous studies [48] have demonstrated the enhancement of dynamic stress–strain behavior and compressive strength in concrete through the addition of carbon fibers (CFs) and carbon nanotubes (CNTs), this study provides unique insights into the synergistic effects of hybrid CF and CNT reinforcement. Specifically, our findings reveal that the combination of CF and CNTs not only enhances dynamic compressive strength but also significantly improves the strain rate effect, which is critical for impact-resistant applications. Additionally, our microstructural analysis highlights the refinement of calcium hydroxide (CH) crystals and the optimization of pore structure, which contribute to a

denser and stronger cement matrix. These findings advance the understanding of how CFs and CNTs can be optimally combined to enhance the performance of concrete in demanding engineering applications.

On the other hand, the incorporation of fibers is a crucial factor in enhancing the mechanical properties of UHPC. Steel fibers are widely used due to their high tensile strength and crack-bridging capability [57]. Studies indicate that increasing SF content from 1% to 3% improves the compressive strength (up to 164 MPa) and significantly enhances tensile and flexural properties. However, steel fibers are the most commonly used fibers in UHPC. The incorporation of steel fibers in UHPC has some disadvantages, such as the potential to corrode, high density (which adds constant load), high cost, and, at high dosages (>4%), SF can lead to workability issues and fiber agglomeration, which may negatively impact mechanical performance [57–59]. This makes it particularly unsuitable for offshore wind turbine foundations, where resistance to harsh marine conditions is crucial Additionally, SF-reinforced UHPC exhibits fracture energy values ranging between 200 and 300 N/m, contributing to its improved ductility.

In comparison, our study explores the potential of carbon fibers (CFs) and carbon nanotubes (CNTs) as alternative reinforcements. Despite using lower reinforcement dosages than typical SF-UHPC mixtures, the combined effect of CFs (9 kg/m^3) and CNTs (0.3% by weight of cement) resulted in a 313% increase in tensile strength compared to the reference mix. Furthermore, fracture energy values reached 291 N/m, placing our system within the expected range for steel fiber-reinforced UHPC. Unlike SF, carbon-based reinforcements also contribute to microstructural densification, improving both durability and resistance to microcracking.

Other fiber types [14], such as polypropylene, polyethylene, and basalt fibers, have also been investigated in UHPC. While synthetic fibers improve fire resistance, they contribute little to compressive or tensile strength enhancements (around 120 MPa). Basalt fibers show moderate increases in mechanical performance (over 20% and 40% growth of compressive and flexural strength [60]) but remain less effective than SFs or CFs in strengthening UHPC. In our study, the synergy between CFs and CNTs provided an optimal balance between tensile strength, fracture resistance, and workability, offering a promising alternative to traditional SF-UHPC systems.

These findings suggest that carbon-based reinforcement can serve as an effective alternative to steel fibers, particularly in applications where high tensile performance and durability are prioritized over maximum compressive strength. Future research should further explore hybrid fiber systems, optimizing combinations of CFs, CNTs, and other additives to achieve tailored mechanical properties in UHPC.

Figure 14 presents a radar chart evaluating the performance of UHPC mixtures across critical parameters: workability, fracture energy, porosity, tensile strength, and compressive strength. Each axis represents a normalized value for these properties, with the outermost polygon (D9-0.54) demonstrating the most balanced and superior performance. The chart highlights how increasing CNT dosage enhances mechanical properties and fracture resistance, albeit with a gradual reduction in workability. Notably, the D9-0.54 mix exhibits the largest area, indicating its optimal overall performance.

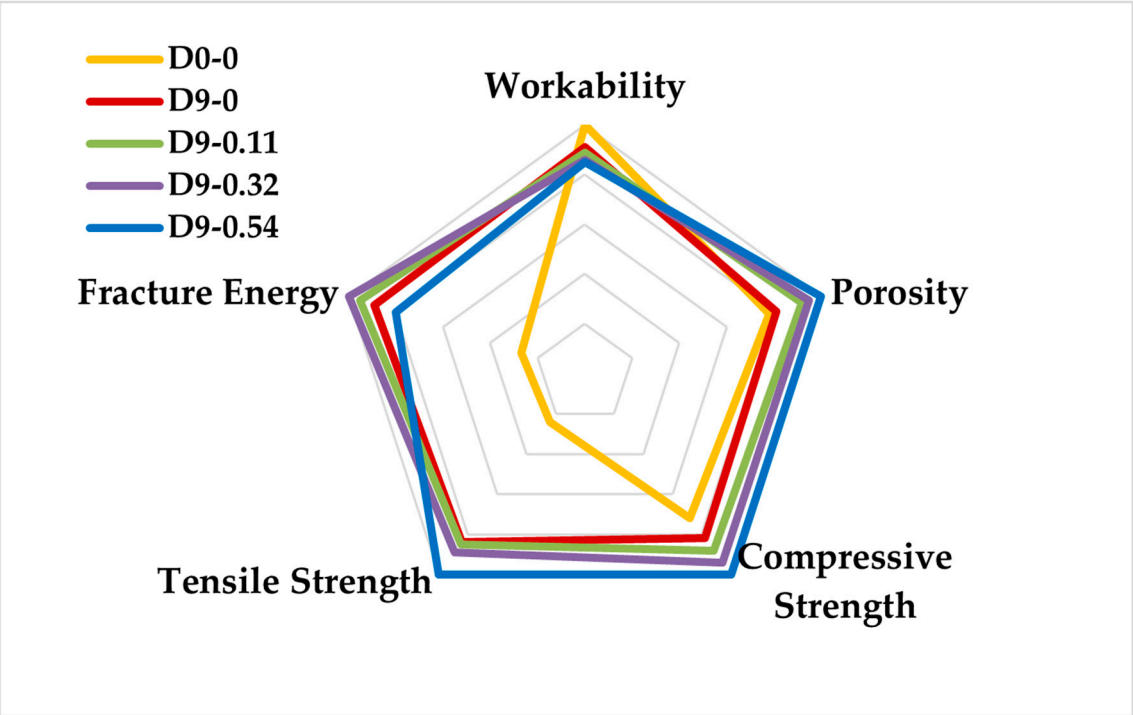


Figure 14. Comparative performance of UHPC mixes.

The D9-0.54 mix (9 kg/m^3 CFs + 0.54 wt% CNTs) achieves the highest scores in compressive strength (24% increase vs. D9-0) and tensile strength (313% increase vs. D0-0), while maintaining acceptable workability (>28 cm slump). Its low porosity (42% reduction vs. D9-0) and high fracture energy (291 N/m) underscore the synergistic effect of CFs and CNTs in refining the microstructure and bridging cracks. This balance positions D9-0.54 as the optimal formulation for applications prioritizing strength, durability, and fracture resistance.

5. Conclusions

- The non-corrosive nature CFs and of CNTs make UHPC a viable and durable material for infrastructure applications, particularly in harsh marine environments, where long-term performance is critical.
- CFs alone achieved a 32% reduction in macro-porosity, while higher concentrations of CNTs (0.54 kg/m^3) further decreased macro-porosity by up to 42%. This resulted in a denser concrete matrix, potentially reducing brittleness and inhibiting crack initiation during fracture. Critically, the CNTs played a key role in refining the UHPC microstructure by filling nanoscale pores, decreasing porosity, and enhancing matrix density, which contributes to improved durability and resistance to internal defects.
- The thermal analysis revealed that CNTs slightly delayed the initial mass loss related to moisture and C–S–H dehydration, attributed to their strengthening of hydration products and formation of denser C–S–H agglomerates. CNTs also increased the mass loss from calcium hydroxide decomposition, indicating their ability to enhance pozzolanic reactions and C–S–H formation.
- CFs play a critical role in crack initiation and propagation. They create a bridging effect that modifies porosity and pore size distribution, enhancing energy absorption during fracture. CNTs also strengthen the bond between aggregates and the cement matrix.
- The synergistic integration of CFs and CNTs significantly enhanced UHPC's mechanical performance—compressive strength increased up to 39% and tensile strength up

to 313% at the highest dosage. Fracture energy also improved with optimized CF (9 kg/m^3) and CNT (0.32 kg/m^3) combinations.

Future research should focus on optimizing CNT dispersion techniques, evaluating the long-term durability of CF- and CNT-reinforced UHPC under real-world conditions, and exploring the use of recycled carbon fibers and sustainable CNT production methods. Additionally, the interaction between CFs, CNTs, and other nanomaterials (e.g., graphene oxide or nano-silica) could be investigated to develop next-generation UHPC with enhanced performance. Large-scale structural testing and field applications are also essential to validate the practical feasibility and economic viability of this material in real-world construction projects.

Author Contributions: Conceptualization, C.L. and H.C.; methodology, J.D.R.; validation, J.D.R.; formal analysis, J.D.R.M.; investigation, J.D.R.M.; data curation, J.D.R.M.; writing—original draft preparation, J.D.R.M.; writing—review and editing, H.C.; visualization, J.D.R.; supervision, C.L.; project administration, H.C.; funding acquisition, H.C. All authors have read and agreed to the published version of the manuscript.

Funding: This research was funded by the "Ministerio de Ciencia e Innovación" of Spain under project numbers PID2019-110928RB-C33 and PID2023-147971OB-C32.

Data Availability Statement: The original contributions presented in the study are included in the article; further inquiries can be directed to the corresponding author.

Acknowledgments: The authors would like to thank Comet Technologies Canada Incorporated for providing the academic license of Dragonfly software.

Conflicts of Interest: The authors declare no conflicts of interest.

References

1. Huang, H.; Teng, L.; Khayat, K.H.; Gao, X.; Wang, F.; Liu, Z. For the Improvement of Mechanical and Microstructural Properties of UHPC with Fiber Alignment Using Carbon Nanotube and Graphite Nanoplatelet. *Cem. Concr. Compos.* **2022**, *129*, 104462. [CrossRef]
2. Bajaber, M.A.; Hakeem, I.Y. UHPC Evolution, Development, and Utilization in Construction: A Review. *J. Mater. Res. Technol.* **2021**, *10*, 1058–1074. [CrossRef]
3. Wang, Y.; Qiao, P.; Sun, J.; Chen, A. Influence of Fibers on Tensile Behavior of Ultra-High Performance Concrete: A Review. *Constr. Build. Mater.* **2024**, *430*, 136432. [CrossRef]
4. Akhnoukh, A.K.; Buckhalter, C. Ultra-High-Performance Concrete: Constituents, Mechanical Properties, Applications and Current Challenges. *Case Stud. Constr. Mater.* **2021**, *15*, e00559. [CrossRef]
5. de Larrard, F.; Sedran, T. Optimization of Ultra-High-Performance Concrete by the Use of a Packing Model. *Cem. Concr. Res.* **1994**, *24*, 997–1009. [CrossRef]
6. Bulte, H.C.; Jiménez, J.R.; Concha, A.M. de la Estudio Del Comportamiento de Hormigones de Muy Alta Resistencia Sometidos a Cargas de Choque Térmico. *Hormig. Acero* **2022**, *73*, 73–79. [CrossRef]
7. Amran, M.; Huang, S.S.; Onaizi, A.M.; Makul, N.; Abdelgader, H.S.; Ozbakkaloglu, T. Recent Trends in Ultra-High Performance Concrete (UHPC): Current Status, Challenges, and Future Prospects. *Constr. Build. Mater.* **2022**, *352*, 129029. [CrossRef]
8. Ríos, J.D.; Leiva, C.; Ariza, M.P.; Seitl, S.; Cifuentes, H. Analysis of the Tensile Fracture Properties of Ultra-High-Strength Fiber-Reinforced Concrete with Different Types of Steel Fibers by X-Ray Tomography. *Mater. Des.* **2019**, *165*, 107582. [CrossRef]
9. Imam, A.; Sharma, K.K.; Kumar, V.; Singh, N. A Review Study on Sustainable Development of Ultra High-Performance Concrete. *AIMS Mater. Sci.* **2022**, *9*, 9–35. [CrossRef]
10. Muñoz-Espinoza, A.L.; López-Yépez, L.G.; Valdez-Aguilar, J.A.; Juarez-Alvarado, C.A.; Durán-Herrera, A. Vitrified Clay for the Production of a Green Sustainable Ultra-High-Performance Fiber-Reinforced Concrete. *Materials* **2024**, *17*, 5624. [CrossRef]
11. Yoo, D.Y.; Banthia, N.; Yoon, Y.S. Recent Development of Innovative Steel Fibers for Ultra-High-Performance Concrete (UHPC): A Critical Review. *Cem. Concr. Compos.* **2024**, *145*, 105359. [CrossRef]
12. He, J.; Chen, W.; Zhang, B.; Yu, J.; Liu, H. The Mechanical Properties and Damage Evolution of UHPC Reinforced with Glass Fibers and High-Performance Polypropylene Fibers. *Materials* **2021**, *14*, 2455. [CrossRef] [PubMed]

13. Chen, Z.; Fan, H.; Zheng, W.; Zhang, S.; Wu, X.; Fu, T.; Yu, D. Influence of Modified PVA Fiber on Ultra-High Performance Concrete and Its Enhancing Mechanism. *Polymers* **2024**, *16*, 3449. [CrossRef]
14. Gong, J.; Ma, Y.; Fu, J.; Hu, J.; Ouyang, X.; Zhang, Z.; Wang, H. Utilization of Fibers in Ultra-High Performance Concrete: A Review. *Compos. B Eng.* **2022**, *241*, 109995. [CrossRef]
15. Pająk, M.; Ponikiewski, T. Flexural Behavior of Self-Compacting Concrete Reinforced with Different Types of Steel Fibers. *Constr. Build. Mater.* **2013**, *47*, 397–408. [CrossRef]
16. Yoo, D.Y.; Kim, S.W.; Park, J.J. Comparative Flexural Behavior of Ultra-High-Performance Concrete Reinforced with Hybrid Straight Steel Fibers. *Constr. Build. Mater.* **2017**, *132*, 219–229. [CrossRef]
17. Patchen, A.; Young, S.; Penumadu, D. An Investigation of Mechanical Properties of Recycled Carbon Fiber Reinforced Ultra-High-Performance Concrete. *Materials* **2023**, *16*, 314. [CrossRef]
18. Xu, S.; Yang, Y.; Wu, C.; Liu, K. Electromagnetic Wave Absorption Performance of UHPC Incorporated with Carbon Black and Carbon Fiber. *Arch. Civ. Mech. Eng.* **2022**, *22*, 71. [CrossRef]
19. Sun, C.S.; Farzana, N.; Kuruppuarachchi, D.; Azimi, M.; Zhong, H. Experimental and Analytical Studies of an Ultra-High Performance Concrete Beam Using Carbon Fiber Reinforced Polymer Bars. *Recent Prog. Mater.* **2023**, *5*, 19. [CrossRef]
20. Wang, X.Q.; Chow, C.L.; Lau, D. Multiscale Perspectives for Advancing Sustainability in Fiber Reinforced Ultra-High Performance Concrete. *Mater. Sustain.* **2024**, *2*, 13. [CrossRef]
21. Huang, H.; Peng, C.; Luo, J.; Sun, T.; Deng, T.; Hu, J.; He, Z.; Wei, J.; Yu, Q.; Anvarovna, K.G.; et al. Micromechanical Properties of Interfacial Transition Zone between Carbon Fibers and UHPC Matrix Based on Nano-Scratching Tests. *Cem. Concr. Compos.* **2023**, *139*, 105014. [CrossRef]
22. Shilar, F.A.; Ganachari, S.V.; Patil, V.B. Advancement of Nano-Based Construction Materials-A Review. *Constr. Build. Mater.* **2022**, *359*, 129535. [CrossRef]
23. Sujitha, V.S.; Ramesh, B.; Xavier, J.R. Effects of Nanomaterials on Mechanical Properties in Cementitious Construction Materials for High-Strength Concrete Applications: A Review. *J. Adhes. Sci. Technol.* **2024**, *38*, 3737–3768. [CrossRef]
24. Ruiz Martinez, J.D.; Cifuentes, H.; Rios, J.D.; Ariza, P.; Leiva, C. Development of Mortars That Use Recycled Aggregates from a Sodium Silicate Process and the Influence of Graphene Oxide as a Nano-Addition. *Materials* **2023**, *16*, 7167. [CrossRef]
25. Ríos, J.D.; Vahí, A.; Leiva, C.; la Concha, A.; Cifuentes, H. Analysis of the Utilization of Air-Cooled Blast Furnace Slag as Industrial Waste Aggregates in Self-Compacting Concrete. *Sustainability* **2019**, *11*, 1702. [CrossRef]
26. Yoo, D.Y.; Oh, T.; Banthia, N. Nanomaterials in Ultra-High-Performance Concrete (UHPC)—A Review. *Cem. Concr. Compos.* **2022**, *134*, 104730. [CrossRef]
27. Wu, Z.; Shi, C.; Khayat, K.H.; Wan, S. Effects of Different Nanomaterials on Hardening and Performance of Ultra-High Strength Concrete (UHSC). *Cem. Concr. Compos.* **2016**, *70*, 24–34. [CrossRef]
28. Jung, M.; Park, J.; Hong, S.-g.; Moon, J. Electrically Cured Ultra-High Performance Concrete (UHPC) Embedded with Carbon Nanotubes for Field Casting and Crack Sensing. *Mater. Des.* **2020**, *196*, 109127. [CrossRef]
29. Jung, M.; Park, J.-s.; Hong, S.G.; Moon, J. Micro- and Meso-Structural Changes on Electrically Cured Ultra-High Performance Fiber-Reinforced Concrete with Dispersed Carbon Nanotubes. *Cem. Concr. Res.* **2020**, *137*, 106214. [CrossRef]
30. Chen, Z.; Lim, J.L.G.; Yang, E.H. Ultra High Performance Cement-Based Composites Incorporating Low Dosage of Plasma Synthesized Carbon Nanotubes. *Mater. Des.* **2016**, *108*, 479–487. [CrossRef]
31. Shah, A.; Chaudhary, M.; Shrestha, J.K. Pattern of Corneal Diseases in Paediatric Age Group at a Tertiary Eye Care Center in Nepal. *Nepal. J. Ophthalmol.* **2017**, *9*, 37–42. [CrossRef] [PubMed]
32. Viana, T.M.; Bacelar, B.A.; Coelho, I.D.; Ludvig, P.; Santos, W.J. Behaviour of Ultra-High Performance Concretes Incorporating Carbon Nanotubes under Thermal Load. *Constr. Build. Mater.* **2020**, *263*, 120556. [CrossRef]
33. Zhang, W.; Zeng, W.; Zhang, Y.; Yang, F.; Wu, P.; Xu, G.; Gao, Y. Investigating the Influence of Multi-Walled Carbon Nanotubes on the Mechanical and Damping Properties of Ultra-High Performance Concrete. *Sci. Eng. Compos. Mater.* **2020**, *27*, 433–444. [CrossRef]
34. Jung, M.; Hong, S.-g.; Moon, J. Ozone Treatment on the Dispersion of Carbon Nanotubes in Ultra-High Performance Concrete. *Mater. Des.* **2020**, *193*, 108813. [CrossRef]
35. Ruan, Y.; Han, B.; Yu, X.; Zhang, W.; Wang, D. Carbon Nanotubes Reinforced Reactive Powder Concrete. *Compos. Part A Appl. Sci. Manuf.* **2018**, *112*, 371–382. [CrossRef]
36. Wang, J.; Dong, S.; Pang, S.D.; Yu, X.; Han, B.; Ou, J. Tailoring Anti-Impact Properties of Ultra-High Performance Concrete by Incorporating Functionalized Carbon Nanotubes. *Engineering* **2022**, *18*, 232–245. [CrossRef]
37. Ríos, J.D.; Cifuentes, H.; Ruiz, G.; González, D.C.; Vicente, M.A.; Yu, R.C.; Leiva, C. Multiscale Analysis of Carbon Microfiber Reinforcement on Fracture Behavior of Ultra-High-Performance Concrete. *Eng. Fract. Mech.* **2025**, *319*, 110998. [CrossRef]
38. Ríos, J.D.; Leiva, C.; de la Concha, A.; Ariza, M.P.; Cifuentes, H. Influence of Graphene Oxide Concentration and Ultrasonication Energy on Fracture Behavior of Nano-Reinforced Cement Pastes. *Crystals* **2024**, *14*, 707. [CrossRef]
39. *EN 12350-2*; Testing Fresh Concrete—Part 2: Slump Test. European Committee for Standardization (CEN): Brussels, Belgium, 2020.

40. Nguyen Amanjean, E.; Mouret, M.; Vidal, T. Effect of Design Parameters on the Properties of Ultra-High Performance Fibre-Reinforced Concrete in the Fresh State. *Constr. Build. Mater.* **2019**, *224*, 1007–1017. [CrossRef]
41. Ríos, J.D.; Cifuentes, H.; Leiva, C.; Seitl, S. Analysis of the Mechanical and Fracture Behavior of Heated Ultra-High-Performance Fiber-Reinforced Concrete by X-Ray Computed Tomography. *Cem. Concr. Res.* **2019**, *119*, 77–88. [CrossRef]
42. *EN-12390-3*; Testing Hardened Concrete—Part 3: Compressive Strength of Test Specimens. European Committee for Standardization (CEN): Brussels, Belgium, 2020.
43. RILEM TCM-85. Determination of the Fracture Energy of Mortar and Concrete by Means of Three-Point Bend Tests on Notched Beams. *Mater. Struct.* **1985**, *18*, 287–290. [CrossRef]
44. Abdalla, H.M.; Karihaloo, B.L. A Method for Constructing the Bilinear Tension Softening Diagram of Concrete Corresponding to Its True Fracture Energy. *Mag. Concr. Res.* **2004**, *56*, 597–604. [CrossRef]
45. Ramachandra Murthy, A.; Karihaloo, B.L.; Iyer, N.R.; Raghu Prasad, B.K. Bilinear Tension Softening Diagrams of Concrete Mixes Corresponding to Their Size-Independent Specific Fracture Energy. *Constr. Build. Mater.* **2013**, *47*, 1160–1166. [CrossRef]
46. Villain, G.; Thiery, M.; Platret, G. Measurement Methods of Carbonation Profiles in Concrete: Thermogravimetry, Chemical Analysis and Gammadensimetry. *Cem. Concr. Compos.* **2007**, *37*, 1182–1192. [CrossRef]
47. Liang, X.; Li, M.; Wang, L.; Liu, S. Effect of Microwave Pretreatment on the Properties and Microstructure of Low-Concentration Carbon Dioxide Early Cured Cement-Based Materials. *Buildings* **2024**, *14*, 1074. [CrossRef]
48. Fu, Q.; Zhou, Z.; Wang, Z.; Huang, J.; Niu, D. Insight into Dynamic Compressive Response of Carbon Nanotube/Carbon Fiber-Reinforced Concrete. *Cem. Concr. Compos.* **2022**, *129*, 104471. [CrossRef]
49. Xu, S.; Wang, J.; Ma, Q.; Wang, L.; Zhang, T. Effect and Mechanism of Two Different Types of Waterproof Admixtures and Silica Fume on the Hydration and Mechanical Properties of Natural Hydraulic Lime. *Case Stud. Constr. Mater.* **2023**, *18*, e01925. [CrossRef]
50. Cifuentes, H.; Leiva, C.; Medina, F.; Fernández-Pereira, C. Effects of Fibres and Rice Husk Ash on Properties of Heated HSC. *Mag. Concr. Res.* **2012**, *64*, 457–470. [CrossRef]
51. Ponikiewski, T.; Katzer, J.; Bugdol, M.; Rudzki, M. Determination of 3D Porosity in Steel Fibre Reinforced SCC Beams Using X-Ray Computed Tomography. *Constr. Build. Mater.* **2014**, *68*, 333–340. [CrossRef]
52. Zeng, J.J.; Hao, Z.H.; Sun, H.Q.; Zeng, W.B.; Fan, T.H.; Zhuge, Y. Durability Assessment of Ultra-High-Performance Concrete (UHPC) and FRP Grid-Reinforced UHPC Plates under Marine Environments. *Eng. Struct.* **2025**, *323*, 119313. [CrossRef]
53. Shah, S.P.; Swartz, S.E.; Ouyang, C. *Fracture Mechanics of Concrete: Applications of Fracture Mechanics to Concrete, Rock and Other Quasi-Brittle Materials*; John Wiley & Sons: Hoboken, NJ, USA, 1995; ISBN 0471303119.
54. Ríos, J.D.; Cifuentes, H.; Leiva, C.; García, C.; Alba, M.D. Behavior of High-Strength Polypropylene Fiber-Reinforced Self-Compacting Concrete Exposed to High Temperatures. *J. Mater. Civ. Eng.* **2018**, *30*, 04018271. [CrossRef]
55. Alyhya, W.S.; Abo Dhaheer, M.S.; Al-Rubaye, M.M.; Karihaloo, B.L. Influence of Mix Composition and Strength on the Fracture Properties of Self-Compacting Concrete. *Constr. Build. Mater.* **2016**, *110*, 312–322. [CrossRef]
56. Bower, A.F.; Ortiz, M. The Influence of Grain Size on the Toughness of Monolithic Ceramics. *J. Eng. Mater. Technol.* **1993**, *115*, 228–236. [CrossRef]
57. Ruiz Martínez, J.D.; Ríos, J.D.; Pérez-Soriano, E.M.; Cifuentes, H.; Leiva, C. Enhancing the Matrix-Fiber Bond in Ultra-High-Performance Fiber-Reinforced Concrete Using a High Performance Plasticizer. Impact on the Flowability, Physical and Mechanical Properties. *Constr. Build. Mater.* **2025**, *470*, 140683. [CrossRef]
58. Yoo, D.Y.; Shin, W.; Chun, B.; Banthia, N. Assessment of Steel Fiber Corrosion in Self-Healed Ultra-High-Performance Fiber-Reinforced Concrete and Its Effect on Tensile Performance. *Cem. Concr. Res.* **2020**, *133*, 106091. [CrossRef]
59. Du, J.; Meng, W.; Khayat, K.H.; Bao, Y.; Guo, P.; Lyu, Z.; Abu-obeidah, A.; Nassif, H.; Wang, H. New Development of Ultra-High-Performance Concrete (UHPC). *Compos. B Eng.* **2021**, *224*, 109220. [CrossRef]
60. Chen, Z.; Wang, X.; Ding, L.; Jiang, K.; Su, C.; Liu, J.; Wu, Z. Mechanical Properties of a Novel UHPC Reinforced with Macro Basalt Fibers. *Constr. Build. Mater.* **2023**, *377*, 131107. [CrossRef]

Disclaimer/Publisher's Note: The statements, opinions and data contained in all publications are solely those of the individual author(s) and contributor(s) and not of MDPI and/or the editor(s). MDPI and/or the editor(s) disclaim responsibility for any injury to people or property resulting from any ideas, methods, instructions or products referred to in the content.